NANO LETTERS

Letter

pubs.acs.org/NanoLett

High-Contrast Terahertz Wave Modulation by Gated Graphene Enhanced by Extraordinary Transmission through Ring Apertures

Weilu Gao,[†] Jie Shu,[†] Kimberly Reichel,[†] Daniel V. Nickel,[†] Xiaowei He,[†] Gang Shi,[‡] Robert Vajtai,[‡] Pulickel M. Ajayan,[‡] Junichiro Kono,[†,‡,§] Daniel M. Mittleman,[†] and Qianfan Xu*[,†]

[†]Department of Electrical and Computer Engineering, [‡]Department of Materials Science and NanoEngineering, and [§]Department of Physics and Astronomy, Rice University, Houston, Texas 77005, United States

ABSTRACT: Gate-controllable transmission of terahertz (THz) radiation makes graphene a promising material for making high-speed THz wave modulators. However, to date, graphene-based THz modulators have exhibited only small on/off ratios due to small THz absorption in single-layer graphene. Here we demonstrate a ~50% amplitude modulation of THz waves with gated single-layer graphene by the use of extraordinary transmission through metallic ring apertures placed right above the graphene layer. The extraordinary transmission induced ~7 times near-filed enhancement of THz absorption in graphene. These results promise complementary metal−oxide−semiconductor compatible THz modulators with tailored operation frequencies, large on/off ratios, and high speeds, ideal for applications in THz communications, imaging, and sensing.

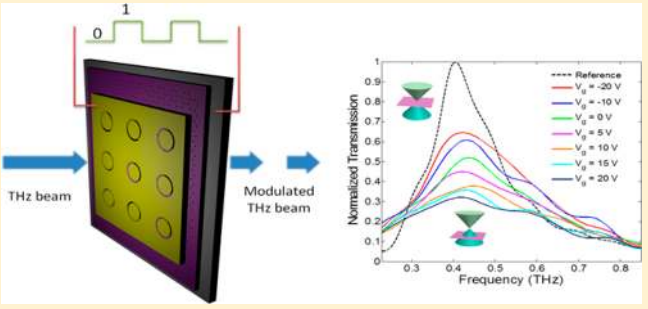

KEYWORDS: *Graphene photonics, THz modulator, extraordinary optical transmission, near-field enhancement, high on/off ratio*

The unique properties of graphene have stimulated worldwide interest in developing novel devices for electronics, photonics, and optoelectronics.[1−3] In particular, gate-controllable electronic properties of graphene are expected to lead to a diverse range of devices,[4] including ultrafast photodetectors,[5,6] transparent electrodes,[7] optical modulators,[8] active plasmonic devices,[9,10] and ultrafast lasers.[11] In the terahertz (THz) frequency region, electrically controllable Drude-like intraband absorption makes graphene a promising platform for building active, graphene-based optoelectronic devices[12−15] such as THz modulators. Compared to THz modulations demonstrated with free carriers in conventional semiconductor materials[16−21] and two-dimensional electron gases in quantum-well structures,[22,23] graphene-based devices have higher carrier mobilities at room temperature with an electrically tunable carrier density.

Despite the broadly tunable carrier density, the extinction ratio that can be obtained for THz wave modulations with single-layer graphene (SLG) is limited due to its one-atomic-layer thickness and the nonresonant nature of the intraband absorption in the THz region. Recently, efforts to enhance the SLG absorption in the THz region have been reported, including exciting plasmonic resonances in graphene,[9] integrating graphene with photonic cavities,[13,14] and integrating graphene with metamaterials.[15,24] However, no devices demonstrated to date have a combination of a large modulation depth, a high speed, and a designable resonance frequency, which we report in this paper.

The extraordinary optical transmission (EOT) effect[18−21] of subwavelength apertures in a metallic film has been used to enhance THz absorption in various materials such as vanadium dioxide (VO_2).[18,20,21] In particular, we previously showed that ring-shaped apertures have a strong polarization-insensitive EOT effect, which allowed us to achieve THz transmission suppression by 18 dB with a thin layer of carriers in a silicon substrate underneath the apertures.[25] Here, we use ring-shaped apertures in a metallic film to enhance the extinction ratio of a graphene-based THz modulator. We show that apertures resonating at ~0.44 THz enhance the intraband absorption in SLG underneath the apertures by ~675%, which leads to a modulation depth of ~50% when the carrier density in SLG is tuned using a back-gating scheme. The modulator has a transmission peak with a bandwidth of ~0.25 THz, which can suppress any off-resonance background signals. By scaling the circumference of the apertures, the operation frequency can be tuned for different applications. In addition, the small gated area and high conductivity of graphene makes high speed and low-energy consumption possible since the aperture-to-area ratio (the ratio of the aperture area to the total metal area) of the EOT structure is only ~1%, and the graphene layer only needs to be present in the area underneath the apertures. These results suggest that complementary metal−oxide−semiconductor (CMOS) compatible THz modulators with tailored operation frequencies, large on/off ratios, and high speeds can be built, which will find a diverse range of applications, including THz communications, imaging, and sensing.[26,27]

Results. The graphene-based THz modulator structure is schematically shown in Figure 1a and b. The EOT THz

Received: November 6, 2013
Revised: February 2, 2014
Published: February 3, 2014

dx.doi.org/10.1021/nl4041274 | *Nano Lett.* 2014, 14, 1242−1248

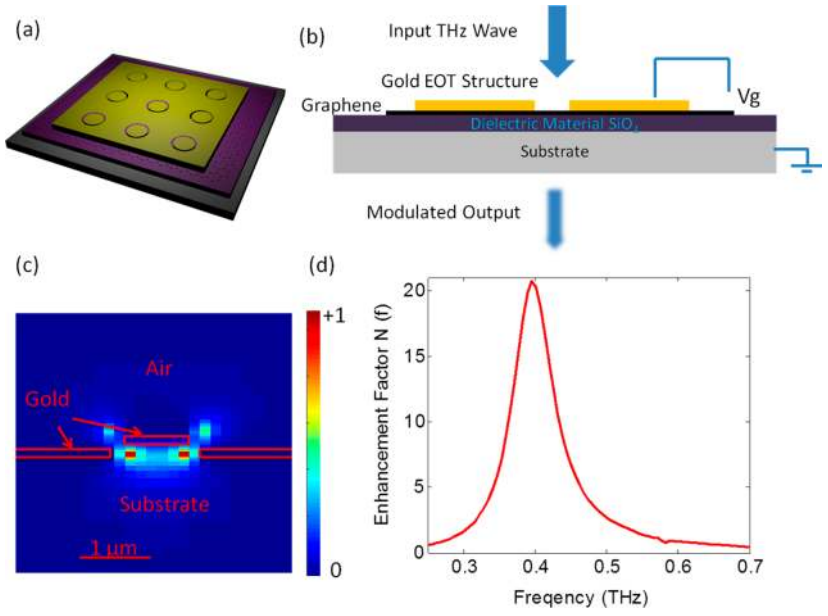

Figure 1. (a) Schematic diagram of the EOT graphene-based THz modulator. (b) Cross section of the EOT graphene-based THz modulator. Graphene is placed on a SiO_2/Si substrate, and the EOT structure is fabricated on top of graphene. The gate voltage is applied between the bottom silicon substrate and the top EOT structure to change the carrier density in graphene. (c) Simulated cross section field distribution of the fabricated gold EOT structure. (d) Absorption enhancement factor $N(f)$ as a function of frequency; at resonance, the enhancement is largest, ~20.

resonator, consisting of an array of ring apertures, is placed on top of the graphene layer, which sits above the dielectric material (SiO_2). EOT is a phenomenon in which a structure containing subwavelength apertures in a metallic film transmits more light than that expected on the basis of ray optics due to a significantly enhanced electric field inside and around the apertures. In the present experiment, a linearly polarized THz wave, normal incident on the ring aperture, excites a bright dipole mode (the TE_{11} mode when the ring aperture is viewed as a coaxial waveguide). At the resonance frequency $f_0 = c/(2\pi r n_{eff})$, where r is the ring radius and n_{eff} is the effective index of the mode, the phase of the radial electric field component E_r of the mode varies by 2π over the circumference of the ring, resulting in a resonant EOT effect; the transmission spectrum of the structure shows a peak at f_0. The electric-field distribution at resonance is shown in Figure 1c, which is a simulation made through the 3D finite difference time domain (FDTD) method using commercial software from Lumerical (see Methods). The near-field enhancement due to EOT will increase the SLG absorption; the absorption enhancement factor $N(f)$, defined by the ratio between the absorption with and without the EOT structure, is proportional to the field intensity near the graphene layer. Since graphene is only a small perturbation for the electrical field, the field distribution in the EOT structure with graphene is assumed to be the same as that of the EOT structure without graphene. Thus, by taking the surface integral of the field intensity over the graphene area, we can obtain the enhancement factor. The largest absorption enhancement factor happens at the resonance frequency f_0 with $N(f_0) \sim 20$, as shown in Figure 1d.

To fabricate the structure illustrated in Figure 1a, we first transferred chemical vapor deposition (CVD) grown graphene from the copper foil onto a SiO_2/Si substrate using standard transfer techniques. The transferred graphene layer was typically p-doped (see Methods).[5,28] The thickness of the SiO_2 layer was chosen to be 90 nm for clear observation[29] of transferred graphene. The silicon substrate as the bottom electrode was lightly doped with a resistivity of ~1−10 Ω·cm. On top of the transferred graphene layer, the EOT structure was made using electron-beam lithography (see Methods). We used a relatively large array size (5×5 mm^2) so that a focused THz beam can fit. The scanning electron microscopy (SEM) images of the fabricated device are shown in Figure 2a, where the bright region is the gold EOT structure and the dark region is graphene underneath. The graphene layer was characterized using Raman spectroscopy, as shown in Figure 2b. The location of the G and 2D peaks (~1590 cm^{-1} and ~2688 cm^{-1}), the single Lorentzian shape of the 2D peak, the 2D/G intensity ratio (>4.0), and the near absence of D peaks all indicate a high-quality SLG sample after the transfer and EOT fabrication processes.[30] The inset of Figure 2a shows one element aperture of the EOT array. The ring diameter is ~96.4 μm, and the aperture width is ~1 μm.

We took THz transmission spectra of the devices using a THz time-domain spectroscopy (THz-TDS) system. Transmission spectra, T_{sp}, for the EOT graphene-based THz modulator under different gate voltages, V_g, from −20 to +20 V were normalized by the reference transmission spectrum, T_{ref}, for the same EOT structure without graphene underneath. The transmission spectra were polarization insensitive, as expected from the structural symmetry. As shown in Figure 2c and d, the peak transmission varied with the gate voltage, while the central frequency remained almost the same at different gate voltages. The transmission change is due to the change in carrier density in graphene as the Fermi level shifts with the gate voltage.[12] We measured a reference device with the same metallic structure on a silicon substrate, but without any graphene underneath. That device showed no obvious change in transmission spectra under different gate voltages, which confirms that any gate-induced effect in the substrate can be neglected. A large modulation depth of ~50% was observed, as shown in Figure 2e, where ΔT is defined as $T(V_g) - T(-20V)$, and it is normalized to the peak of $T(-20V)$ at the center frequency. The corresponding transmission phase spectra are plotted in Figure 2f, which indicate that the amount of gate-induced phase modulation is not very large.

dx.doi.org/10.1021/nl4041274 | Nano Lett. 2014, 14, 1242−1248

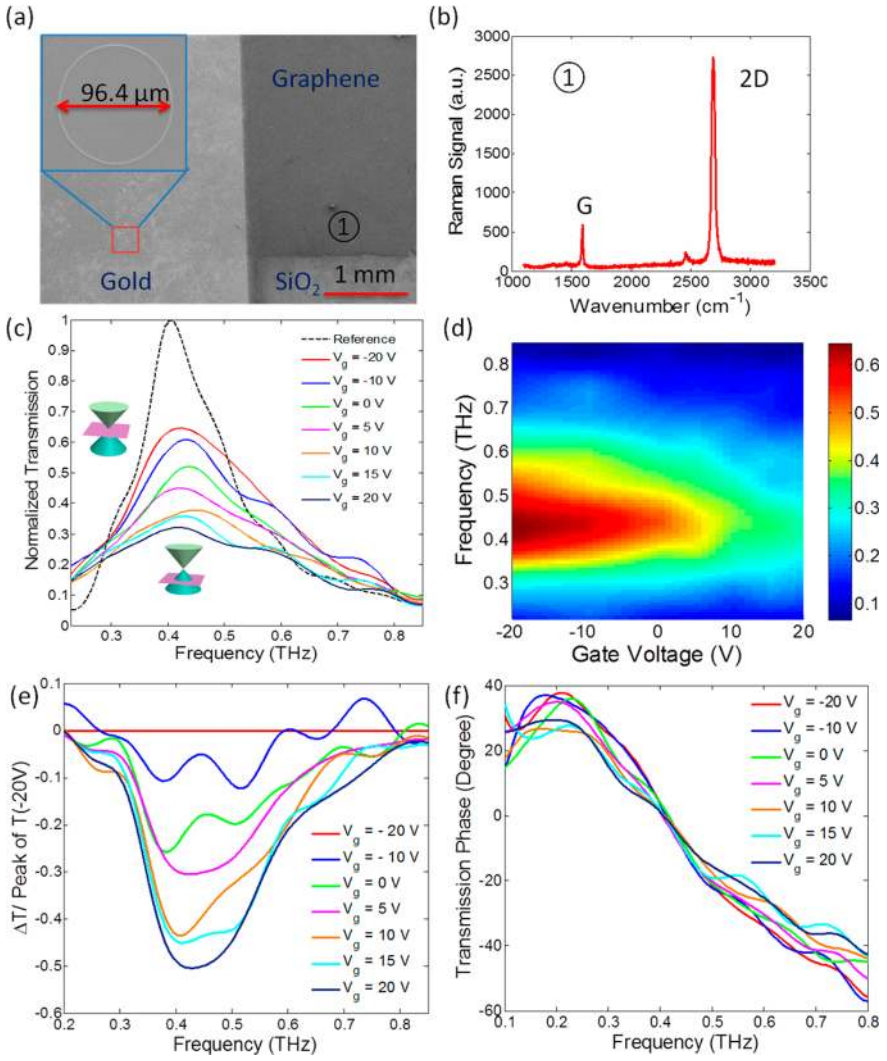

Figure 2. (a) Scanning electron microscopy image of the fabricated EOT-graphene-based THz modulator on the SiO_2/Si substrate. The dark region is graphene underneath. The scale bar is 1 mm. The inset is one EOT ring aperture element of the array. (b) Raman spectrum of graphene underneath the EOT structure. (c) Transmission spectra for the EOT graphene-based THz modulator under different gate voltages between −20 V and +20 V. The peak transmission changes more than a factor of 2. (d) The transmission spectra versus gate voltage plotted in a 2D color map. (e) The transmission change at different gate voltages. A large modulation depth of ∼50% is obtained. (f) The transmission phase spectra at different gate voltages.

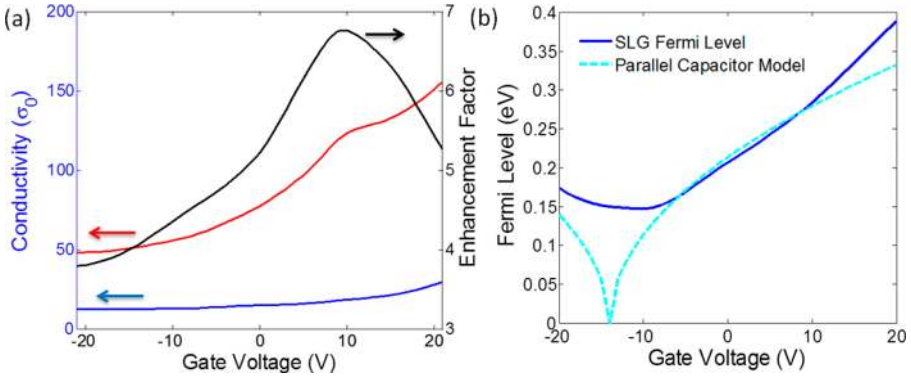

Figure 3. (a) Real part of the conductivity with the EOT structure (red line) at the resonance frequency compared with that of SLG without EOT structure (blue line) and the enhancement factor (black line) as a function of gate voltage. The largest enhancement factor is ∼7. (b) Fermi level of graphene as a function of gate voltage estimated using two different methods. The blue solid line is from SLG THz absorption measurement,[12] and the cyan dashed line is from calculation using eq 1.

The Drude-like absorption in SLG has been previously investigated from the THz to the mid-infrared region.[12,31] In comparison, the absorption, which is proportional to the real part of the complex conductivity (in units of $\sigma_0 = e^2/4\hbar$), observed at

dx.doi.org/10.1021/nl4041274 | Nano Lett. 2014, 14, 1242−1248

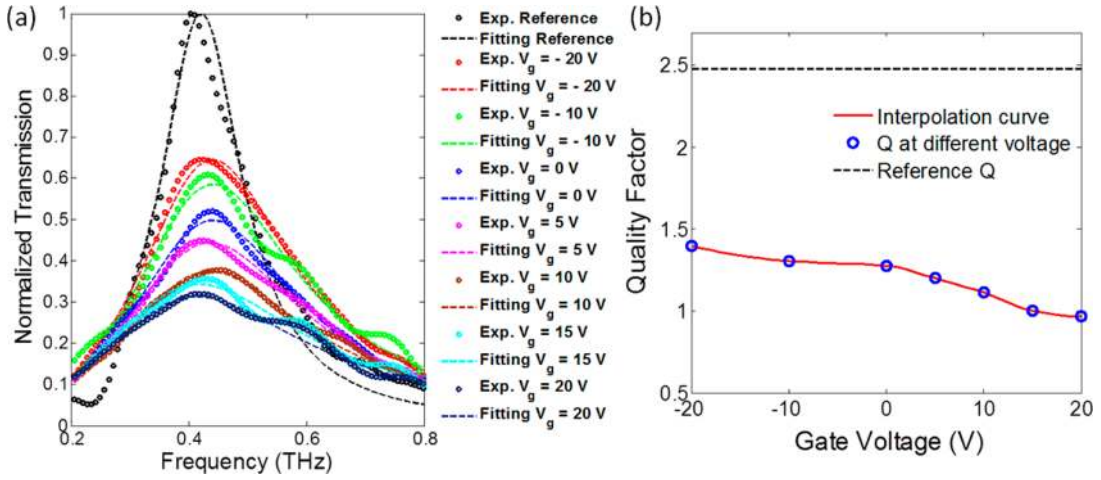

Figure 4. (a) Normalized transmission spectra at different gate voltages, each spectrum is fitted with eq 2. The black line represents the reference structure. (b) Quality factor versus gate voltage obtained through fitting shown in (a). The black dashed line is the *Q*-factor of the reference sample.

the resonance frequency in our experiment is about seven times stronger, as shown in Figure 3a. This enhancement is mainly due to the strong near-field enhancement near the ring apertures, which strengthens the interaction between the THz field and SLG (see Methods). The enhancement is not as high as that expected from the simulation shown in Figure 1d; the possible reasons include imperfection of fabrication that may lead to partial closing of the ring aperture, absorption loss from residual resist, and nonuniformity of graphene carrier distribution over the large area.[32]

As the gate voltage approaches the largest reverse bias voltage of −20 V limited by the breakdown of the SiO_2 layer, the THz absorption by the SLG approaches a nonzero value, as the red line in Figure 3a shows. This implies that there will still be a finite THz conductivity in SLG even when the Fermi level approaches the Dirac point. We believe that this is due to the nonuniformity in the Fermi level in large-area graphene. Since the entire area cannot reach the Dirac point at the same bias voltage, there are always residual carriers in the film that induces residual THz loss.[12]

The average carrier density in large-area SLG without the EOT structure can be extracted by fitting the measured transmission spectrum with the Drude model (see Methods).[12] When the gate voltage is swept from −20 to +20 V, the Fermi level in SLG without EOT structure is expected to change by a factor of 2, as shown by the blue solid line in Figure 3b. The Fermi level of graphene can be estimated using the parallel capacitor model as[12]

$$|E_f(V_g)| = \hbar v_f \sqrt{\pi \alpha_c |V_g - V_{CNP}|} \quad (1)$$

where $E_f(V_g)$ is the Fermi level at gate voltage V_g, $\hbar$ is the reduced Planck constant, v_f is the Fermi velocity ($\sim 10^6$ m/s), α_c is a capacitor constant ($= 2.4 \times 10^{11}$ cm^{-2} V^{-1} in our case), and V_{CNP} is taken as ~ -14 V (see Methods). The calculated Fermi level is shown by the cyan dashed line in Figure 3b. However, compared with theoretical calculation, the Fermi level should come to the Dirac point at the charge neutral point (i.e., CNP, which is the voltage shifting the graphene Fermi level to the Dirac point), while in our case there are always residual carriers and strong asymmetry between holes and electrons in SLG as shown by the blue solid line in Figure 3b. Possible reasons include the nonuniform carrier distribution due to defects in the substrate or grain boundaries of polycrystalline graphene[32,33] and hole-rich puddles[34] from the transfer and fabrication processes (see Methods).

In the EOT-graphene structure, graphene can be viewed as an electrically controlled decay channel in an EOT resonant cavity. The transmission spectrum can be fit using a Lorentzian function inferred from coupled mode theory[35] as

$$T(f) = \frac{A}{(f - f_0)^2 + \Gamma^2} \quad (2)$$

where f_0 is the resonance frequency, A is the amplitude, and Γ is the line width taking into account the combined losses from the metal and graphene, which can be expressed as $\alpha\ \mathrm{Im}(\varepsilon_{gra}) + \beta\ \mathrm{Im}(\varepsilon_{gold})$, where ε_{gra} and ε_{gold} are the graphene and gold dielectric functions, respectively, α and β are scaling factors; we assume that the graphene term changes with the gate voltage while the gold term remains constant.[36] The two dielectric functions can be expressed using the Drude model. Specifically, $\varepsilon_{gra} = 1 + i\sigma_{gra}/\omega\varepsilon_0 t_{gra}$, where σ_{gra} is the SLG Drude conductivity (see Methods) and t_{gra} is the graphene thickness (taken as 0.34 nm for SLG) while $\varepsilon_{gold} = 1 - (\omega_p^2/\omega(\omega + i\gamma_{gold}))$, where $\omega_p/2\pi$ is the plasma frequency of gold (taken as 2180 THz[37]) and $\gamma_{gold}/2\pi$ is the scattering rate of gold (taken as 6.45 THz[37]). The spectrum shown in Figure 2c can be well fit by eq 2, as shown in Figure 4a. A slight discrepancy between the measured and the fitting spectra is attributed to imperfect fabrication of the EOT structure. The quality factor (*Q*-factor) extracted from the fitted spectrum in Figure 4a decreases as the carrier density increases in graphene, which introduces a higher loss in the EOT resonator. Compared to the reference structure that was built without graphene (shown by the black dashed line in Figure 4b), the *Q*-factor decreases due to the graphene insertion loss caused by the residual carriers.

Our EOT-graphene-based THz modulator can potentially operate with speeds on the order of hundreds of MHz, primarily due to the small aperture-to-area ratio of the EOT structure. In this structure, graphene only needs to be present in the aperture to have an effect. If we assume that the beam size of the THz wave is ~ 1 mm^2 and the aperture-to-area ratio is $\sim 1\%$, the total area of graphene, A_{gra}, needed for effective amplitude modulation is ~ 0.01 mm^2. Here we can estimate the potential speed of our device structure. The modulation speed is limited by the *RC* of the circuit, where R (C) is the resistance (capacitance). In our back-gating scheme, the fundamental limitation of the device

dx.doi.org/10.1021/nl4041274 | *Nano Lett.* 2014, 14, 1242−1248

capacitance is attributed to the graphene area, which can be calculated as $C = \varepsilon_0\varepsilon_d A_{gra}/d \approx 3.8$ pF, where ε_d (= 3.9) is the relative permittivity of silicon oxide, ε_0 is the vacuum permittivity, and d (= 90 nm) is the thickness of silicon oxide. The parasitic capacitance from the metal film can be significantly reduced by placing it much farther away from the silicon layer, for example, by placing a thicker dielectric layer (such as SiO_2) underneath the metal. The resistance mainly comes from the graphene resistance and the contact resistance; the former is typically several kilo-ohms in our devices and the latter is several ohms. However, in highly doped graphene, the resistance can be as low as ~125 Ω/sq, which will reduce the resistance involved in the device.[7,36] Thus, the speed, taken as $1/2\pi RC$, can be as large as ~0.2 GHz by taking $R \sim 200$ Ω.

In conclusion, we have demonstrated a new type of active transmissive THz modulator based on graphene. Because of the near-field enhancement of THz absorption in graphene due to EOT through metallic ring apertures placed right above the graphene layer, a strong amplitude modulation with a depth as large as ~50% was achieved. Its operation speed is expected to be up to hundreds of MHz, and its modulation depth can be further improved by better device fabrication and higher graphene quality. Furthermore, the EOT array can be scaled to have resonance frequencies over a wide THz range; it can also be pixelated to have independently controllable subarrays, which will enable a high-speed on-chip THz spatial light modulator with low bias voltage at room temperature. Our results thus suggest that a room temperature, CMOS-compatible THz modulator with a large on/off ratio, high speed, and tailored working frequency can be developed with future application in THz communications, imaging, and sensing.

Methods. *Device Fabrication.* The graphene layer was grown by chemical vapor deposition (CVD) on copper foil and then transferred onto a SiO_2/Si substrate using a poly(methyl methacrylate) (PMMA) assisted wet-transfer technique.[5,28] In this transfer process, first a PMMA layer was spin-coated on graphene on the copper foil, and the copper foil was then etched away in 10% nitric acid overnight. The PMMA-graphene film floating on the etchant was moved to distilled water several times to rinse the etchant residue and then scooped by the substrate. The chip was dried in air overnight, and the PMMA was removed by acetone, and the whole chip was cleaned by isopropyl alcohol (IPA). The EOT array was then defined on top of the graphene layer using electron beam lithography (JEOL-6500) with double layer resists facilitating the lift-off process. The first layer was water-soluble OmniCoat coated on the transferred graphene substrate, and then SU-8 was spin-coated over OmniCoat. After developing the top SU-8 layer using the SU-8 developer, the OmniCoat was developed by a wet etching method using MF-319 with carefully controlled time. Finally, 3-nm-thick titanium and 97-nm-thick gold were successively evaporated using electron beam evaporator, and the metal layers were lifted off using PG remover. The lift-off process was not completely successful, and there was still some metal covering the top and sidewall of the aperture. However, the sidewall was not fully covered by gold, and the EOT effect through such structures still gave a clear resonance in transmission spectra, as shown in Figure 2c.

3D FDTD Simulation. We performed a 3D finite-difference-time-domain (FDTD) simulation using Lumerical FDTD software. The simulated structure consisted of ring aperture arrays in a gold film with a thickness of h = 100 nm on an intrinsic silicon substrate, which is excited by a normal-incident broadband THz wave polarized along the horizontal direction, as shown in Figure 1c. The ring apertures have a radius of r = 50 μm and a width of w = 1 μm. The periodic boundary conditions were used, assuming a square-lattice array with the lattice constant p = 150 μm. Considering the imperfection of the fabricated device having the metal on top of resist SU8 due to the imperfect lift-off process, in the simulations we added a 500-nm-thick dielectric layer with a refractive index of 1.46 inside the ring aperture, with another 100-nm-thick gold layer on top.

SLG Drude Conductivity. Transmission spectra of bare SLG without the EOT structure normalized to bare SiO_2/Si wafer from the THz to the mid-infrared can be used to extract the Fermi level as the following[12]

$$T = \frac{1}{\{1 + [\pi\alpha/(1 + n_{sub})][\sigma(E_f)/\sigma_0]\}^2} \quad (3)$$

where α is the fine structure constant, n_{sub} (= 3.42) is the refractive index of the substrate, $\sigma_0 = e^2/4\hbar$ is the universal optical conductivity in graphene, $\sigma(E_f)$ is the real part of graphene conductivity from the Drude model, $\sigma_g(\omega,) = ie^2E_f/\pi\hbar^2(\omega + i/\tau)$, where e is the electronic charge, E_f is the Fermi level, and τ is the carrier scattering time of carriers. The large-area graphene Fermi level under different voltages was retrieved from ref 12 and scaled to 90 nm silicon oxide dielectrics. Similarly, the transmission peak change of SLG with EOT structure normalized to the EOT structure without graphene as dashed line in Figure 2c can be used to extract the equivalent graphene conductivity with strong-field enhancement by EOT structure, and the ratio of these two conductivity (with and without structure) will be the enhancement factor. The charge neutrality point of graphene is estimated around −14 V from typical field effect transistor (FET) measurements and transmission spectrum fitting of intrinsically doped graphene without any bias using eq 3.

Statistic Model of Large-Area SLG Nonuniformity. Possible reasons for residual THz absorption for SLG is the nonuniformity of large area graphene CNP, which may be from defects in substrates, polycrystalline graphene characteristics, and fabrication process; thus the nominal Fermi level extracted from the Drude model fitting absorption is the average response over the large area of several millimeters of the THz beam spot. Here we model this nonuniformity by assuming a statistic normal distribution of CNP[34] over the large area to get the average carrier density, that is, the nominal Fermi level (see Methods) as

$$|E_f(V_g)| = \hbar v_f\sqrt{\pi\alpha_c|V_g - \tilde{V}_{CNP}|} \quad (4)$$

where the charge neutral point $\tilde{V}_{CNP}$ follows the normal distribution $\tilde{V}_{CNP} \sim N(\mu,\sigma)$. The nominal Fermi level can be obtained by taking the average of Fermi level when CNP changes statistically according to normal distribution using the Monte Carlo method. In our case, the expectation μ is chosen as −14 V and the deviation σ is fitted ~8.5 V, corresponding to a CNP shift of ~0.166 eV by fitting the blue solid line in Figure 3b, which indicates that the large-area graphene has significant nonuniformity compared with small-area graphene.[34] The relationship between the average Fermi level and gate voltage is shown as the red solid line in Figure 5, which matches well with the SLG Fermi level from the Drude model fitting as the blue solid line in Figure 5.

dx.doi.org/10.1021/nl4041274 | Nano Lett. 2014, 14, 1242−1248

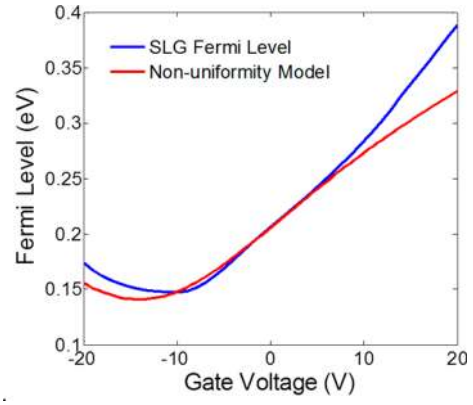

Figure 5. Statistic model fitting for large-area graphene Fermi level tuning.

AUTHOR INFORMATION

Corresponding Author

*E-mail: qianfan@rice.edu.

Author Contributions

W.G. and J.S. contributed equally to this work.

Notes

The authors declare no competing financial interest.

ACKNOWLEDGMENTS

This work was partially supported by the Air Force Office of Scientific Research (AFOSR) Grant FA9550-12-1-0261 and the National Science Foundation (through Grant No. ECCS-1308014). K.R, D.V.N., and D.M.M. acknowledge partial support from the National Science Foundation. X.H. and J.K. acknowledge support from the Department of Energy (through Grant No. DE-FG02-06ER46308), the National Science Foundation (through Grants No. OISE-0968405 and EEC-0540832), and the Robert A. Welch Foundation (through Grant No. C-1509). G.S., R.V., and P.M.A. acknowledge the support provided by NSF-PIRE Grant No. OISE-0968405 and the funds provided by US Office of Naval Research (MURI grant N000014-09-1-1066).

REFERENCES

(1) Castro Neto, A. H.; Guinea, F.; Peres, N. M. R.; Novoselov, K. S.; Geim, A. K. *Rev. Mod. Phys.* **2009**, *81* (1), 109−162.

(2) Geim, A. K.; Novoselov, K. S. *Nat. Mater.* **2007**, *6* (3), 183−191.

(3) Novoselov, K. S.; Geim, A. K.; Morozov, S. V.; Jiang, D.; Zhang, Y.; Dubonos, S. V.; Grigorieva, I. V.; Firsov, A. A. *Science* **2004**, *306* (5696), 666−669.

(4) Bonaccorso, F.; Sun, Z.; Hasan, T.; Ferrari, A. C. *Nat. Photonics* **2010**, *4* (9), 611−622.

(5) Xia, F. N.; Mueller, T.; Lin, Y. M.; Valdes-Garcia, A.; Avouris, P. *Nat. Nanotechnol.* **2009**, *4* (12), 839−843.

(6) Vicarelli, L.; Vitiello, M. S.; Coquillat, D.; Lombardo, A.; Ferrari, A. C.; Knap, W.; Polini, M.; Pellegrini, V.; Tredicucci, A. *Nat. Mater.* **2012**, *11* (10), 865−871.

(7) Bae, S.; Kim, H.; Lee, Y.; Xu, X. F.; Park, J. S.; Zheng, Y.; Balakrishnan, J.; Lei, T.; Kim, H. R.; Song, Y. I.; Kim, Y. J.; Kim, K. S.; Ozyilmaz, B.; Ahn, J. H.; Hong, B. H.; Iijima, S. *Nat. Nanotechnol.* **2010**, *5* (8), 574−578.

(8) Liu, M.; Yin, X. B.; Ulin-Avila, E.; Geng, B. S.; Zentgraf, T.; Ju, L.; Wang, F.; Zhang, X. *Nature* **2011**, *474* (7349), 64−67.

(9) Ju, L.; Geng, B. S.; Horng, J.; Girit, C.; Martin, M.; Hao, Z.; Bechtel, H. A.; Liang, X. G.; Zettl, A.; Shen, Y. R.; Wang, F. *Nat. Nanotechnol.* **2011**, *6* (10), 630−634.

(10) Yan, H. G.; Li, X. S.; Chandra, B.; Tulevski, G.; Wu, Y. Q.; Freitag, M.; Zhu, W. J.; Avouris, P.; Xia, F. N. *Nat. Nanotechnol.* **2012**, *7* (5), 330−334.

(11) Sun, Z. P.; Hasan, T.; Torrisi, F.; Popa, D.; Privitera, G.; Wang, F. Q.; Bonaccorso, F.; Basko, D. M.; Ferrari, A. C. *ACS Nano* **2010**, *4* (2), 803−810.

(12) Ren, L.; Zhang, Q.; Yao, J.; Sun, Z. Z.; Kaneko, R.; Yan, Z.; Nanot, S.; Jin, Z.; Kawayama, I.; Tonouchi, M.; Tour, J. M.; Kono, J. *Nano Lett.* **2012**, *12* (7), 3711−3715.

(13) Sensale-Rodriguez, B.; Yan, R. S.; Kelly, M. M.; Fang, T.; Tahy, K.; Hwang, W. S.; Jena, D.; Liu, L.; Xing, H. G. *Nat. Commun.* **2012**, *3*, 780.

(14) Sensale-Rodriguez, B.; Yan, R. S.; Rafique, S.; Zhu, M. D.; Li, W.; Liang, X. L.; Gundlach, D.; Protasenko, V.; Kelly, M. M.; Jena, D.; Liu, L.; Xing, H. G. *Nano Lett.* **2012**, *12* (9), 4518−4522.

(15) Lee, S. H.; Choi, M.; Kim, T. T.; Lee, S.; Liu, M.; Yin, X.; Choi, H. K.; Lee, S. S.; Choi, C. G.; Choi, S. Y.; Zhang, X.; Min, B. *Nat. Mater.* **2012**, *11* (11), 936−941.

(16) Chen, H. T.; Padilla, W. J.; Zide, J. M. O.; Gossard, A. C.; Taylor, A. J.; Averitt, R. D. *Nature* **2006**, *444* (7119), 597−600.

(17) Chan, W. L.; Chen, H. T.; Taylor, A. J.; Brener, I.; Cich, M. J.; Mittleman, D. M. *Appl. Phys. Lett.* **2009**, *94* (21), 213511.

(18) Seo, M.; Kyoung, J.; Park, H.; Koo, S.; Kim, H. S.; Bernien, H.; Kim, B. J.; Choe, J. H.; Ahn, Y. H.; Kim, H. T.; Park, N.; Park, Q. H.; Ahn, K.; Kim, D. S. *Nano Lett.* **2010**, *10* (6), 2064−2068.

(19) Seo, M. A.; Park, H. R.; Koo, S. M.; Park, D. J.; Kang, J. H.; Suwal, O. K.; Choi, S. S.; Planken, P. C. M.; Park, G. S.; Park, N. K.; Park, Q. H.; Kim, D. S. *Nat. Photonics* **2009**, *3* (3), 152−156.

(20) Chen, H. T.; Lu, H.; Azad, A. K.; Averitt, R. D.; Gossard, A. C.; Trugman, S. A.; O'Hara, J. F.; Taylor, A. J. *Opt. Express* **2008**, *16* (11), 7641−7648.

(21) Hendry, E.; Lockyear, M. J.; Rivas, J. G.; Kuipers, L.; Bonn, M. *Phys. Rev. B* **2007**, *75* (23), 235305.

(22) Kersting, R.; Strasser, G.; Unterrainer, K. *Electron. Lett.* **2000**, *36* (13), 1156−1158.

(23) Libon, I. H.; Baumgartner, S.; Hempel, M.; Hecker, N. E.; Feldmann, J.; Koch, M.; Dawson, P. *Appl. Phys. Lett.* **2000**, *76* (20), 2821−2823.

(24) Papasimakis, N.; Luo, Z. Q.; Shen, Z. X.; De Angelis, F.; Di Fabrizio, E.; Nikolaenko, A. E.; Zheludev, N. I. *Opt. Express* **2010**, *18* (8), 8353−8359.

(25) Shu, J.; Qiu, C. Y.; Astley, V.; Nickel, D.; Mittleman, D. M.; Xu, Q. F. *Opt. Express* **2011**, *19* (27), 26666−26671.

(26) Kleine-Ostmann, T.; Pierz, K.; Hein, G.; Dawson, P.; Koch, M. *Electron. Lett.* **2004**, *40* (2), 124−126.

(27) Chan, W. L.; Charan, K.; Takhar, D.; Kelly, K. F.; Baraniuk, R. G.; Mittleman, D. M. *Appl. Phys. Lett.* **2008**, *93* (12), 121105.

(28) Suk, J. W.; Kitt, A.; Magnuson, C. W.; Hao, Y. F.; Ahmed, S.; An, J. H.; Swan, A. K.; Goldberg, B. B.; Ruoff, R. S. *ACS Nano* **2011**, *5* (9), 6916−6924.

(29) Blake, P.; Hill, E. W.; Neto, A. H. C.; Novoselov, K. S.; Jiang, D.; Yang, R.; Booth, T. J.; Geim, A. K. *Appl. Phys. Lett.* **2007**, *91* (6), 063124.

(30) Ferrari, A. C.; Meyer, J. C.; Scardaci, V.; Casiraghi, C.; Lazzeri, M.; Mauri, F.; Piscanec, S.; Jiang, D.; Novoselov, K. S.; Roth, S.; Geim, A. K. *Phys. Rev. Lett.* **2006**, *97* (18), 187401.

(31) Horng, J.; Chen, C. F.; Geng, B. S.; Girit, C.; Zhang, Y. B.; Hao, Z.; Bechtel, H. A.; Martin, M.; Zettl, A.; Crommie, M. F.; Shen, Y. R.; Wang, F. *Phys. Rev. B* **2011**, *83* (16), 165113.

(32) Buron, J. D.; Petersen, D. H.; Boggild, P.; Cooke, D. G.; Hilke, M.; Sun, J.; Whiteway, E.; Nielsen, P. F.; Hansen, O.; Yurgens, A.; Jepsen, P. U. *Nano Lett.* **2012**, *12* (10), 5074−5081.

(33) Niesner, D.; Fauster, T.; Dadap, J. I.; Zaki, N.; Knox, K. R.; Yeh, P. C.; Bhandari, R.; Osgood, R. M.; Petrovic, M.; Kralj, M. *Phys. Rev. B* **2012**, *85* (8), 081402.

(34) Martin, J.; Akerman, N.; Ulbricht, G.; Lohmann, T.; Smet, J. H.; Von Klitzing, K.; Yacoby, A. *Nat. Phys.* **2008**, *4* (2), 144−148.

(35) Gan, X. T.; Mak, K. F.; Gao, Y. D.; You, Y. M.; Hatami, F.; Hone, J.; Heinz, T. F.; Englund, D. *Nano Lett.* **2012**, *12* (11), 5626−5631.

(36) Majumdar, A.; Kim, J.; Vuckovic, J.; Wang, F. *Nano Lett.* **2013**, *13* (2), 515−518.

(37) *Handbook of terahertz technology for imaging, sensing and communications*. Daryoosh, S., Ed.; Elsevier: Waterloo, Canada, 2013; p 65.